Polymer nanocomposite film based piezoelectric nanogenerator for biomechanical energy harvesting and motion monitoring

Shilpa Rana[1], and Bharti Singh[1,*]

[1] Department of Applied Physics, Delhi Technological University, Main Bawana Road, Delhi 110042, India

ABSTRACT

With the advancement in the wearable technologies such as, smart watches, electronic skin, and wearable portable device, scavenging the biomechanical energy from human movements have gained considerable attention for designing self-sustainable power system. Here, we have reported a flexible piezoelectric device that can be conformably adhered to the human body in order to harness the energy from diversification of touch and motion. For this, we have fabricated a polyvinyl difluoride (PVDF) polymer based flexible piezoelectric nanogenerator (PNG) device that can harness energy from various human motions and convert it to useful electrical energy. To further improve the performance of PVDF based nanogenerator, hydrothermally synthesized nanosheets of reduce graphene oxide (rGO) and boron doped rGO are embedded in PVDF matrix as a conductive nanofiller materials to enhance the device output performance. Among all fabricated devices based on pristine PVDF (P), rGO doped PVDF (PR) and, boron doped rGO (PBR), the latter generates a maximum voltage and power density of 13.8 V and ~ 42.3 $\mu W/cm^2$ respectively, which is then used to light up series of commercially available LEDs. Finally, PBR film based PNG is demonstrated to harvest energy from different types of human motion which includes finger tapping, elbow bending, foot tapping, leg folding, and wrist movements. This device demonstrates the potential use of polymer nanocomposite films in self-powered wearable devices.

1 Introduction

With the technological advancement, flexible, wearable and, miniaturized microelectronic devices with diverse functionality are rapidly becoming the part of our mundane life by affecting various aspects of human life from health monitoring, and entertainment to information and communication technology [1, 2]. One of the important factors for continuous and stable operation of these flexible and wearable electronic devices is the sustainable power supply. Till now, batteries have been used as one of the most reliable and economical sources to supply power to these electronic devices but their frequent recharging and replacement process, bulky nature and disposal difficulty are becoming challenge for their long term application and environmental safety [3, 4].

Address correspondence to E-mail: bhartisingh@dtu.ac.in

This problem can be overcome by scavenging the energy from our living environment as there are ample green sources of energy present in our environment including motion or movements, vibrations, waves, solar energy, wind, and thermal energy sources which are capable of generating electricity [5–8]. Among which scavenging mechanical energy particularly from the human body, where sufficient energy is generated by human motion can become potential alternative to supply power to the portable, and wearable electronic device. In this regard, piezoelectric nanogenerators (PNG) have gathered significant attention because of their outstanding ability to convert tiny and irregular mechanical energy from running, walking, typing, muscle movements, and respiration etc. into electricity with the help of piezoelectric materials [9–12]. Several PNG have been developed over the past few years using PZT, $BaTiO_3$, GaN, $LiNbO_3$, PVDF, and its copolymers to increase the energy conversion efficiency since the invention of first PNG by Prof. Zhong Lin Wang group in 2006 [13–17]. However, inorganic piezoelectric materials suffer from poor toughness/ brittleness, low durability, toxicity and heavy weight which restrict their application in flexible piezoelectric energy harvesting device. In this regard, piezoelectric polymer for example PVDF and its copolymer is a good choice for fabricating flexible nanogenerator due to its flexible, lightweight, biocompatibility, and conformable nature makes them favorable to design flexible device. The electroactive polar (i.e. β and γ) phases are responsible for facilitating the piezoelectric properties in PVDF film. The piezoelectric response of the PVDF can be further enhanced by several mechanisms, such as, electric poling, mechanical stretching, and the addition of nanofillers i.e. carbon based materials, metal nanoparticles (NPS), metal oxide, and ceramics in polymer matrix which helps in nucleation of electroactive polar phase [16, 18]. Anand et al. synthesized the PVDF composite films via the solution casting method in which addition of rGO in the PVDF matrix and applying the UV Visible light exposure on the sample enhances the piezoresponse of the polymer composite films upto 8 times in comparison to pristine PVDF film and hence producing a maximum voltage of ~ 1.9 V [19]. Hu et al. fabricated a wearable piezoelectric nanogenerator using rGO/PVDF-TrFE film and uses in situ polarization method to increase the energy harvesting performance of the device [20]. The fabricated nanogenerator can produce a maximum voltage, current, and power density of 8.3 V, 0.6 μA, and 28.7 W/m^3 respectively. Also, it has been observed from the literature that doping of

rGO with other atoms, such as Fe reported by Karan et al. increases the output performance of the PENG by enhancing the electrical properties [21]. In the reported work, the addition of Fe doped rGO not only helps in the nucleation of electroactive γ phase to ~ 99% (± 0.18 of relative proportion) in PVDF but also increases the surface conductivity up to ~ 3.30×10^{-3} Scm^{-1} as a result enhance piezoelectric properties of nanocomposite films. Also, the doping of nitrogen, iron, and co-doping of two different heteroatoms in rGO are also reported to enhances the piezoelectric performance of PVDF based nanocomposite film [22, 23]. However, studies on the enhancement of piezoelectric properties in boron doped rGO (B-rGO) have been found to be relatively limited. Furthermore, boron doping in rGO framework leads to redistribution of the energy density, which alters the band structure, charge transfer characteristics, and electronic properties, facilitating it applications in numerous fields, such as, supercapacitors [24], batteries [25], solar cell [26], biomedical applications [27, 28] and can also affects the piezoelectric response of rGO.

In the current study, we have reported a flexible PVDF composite film based piezoelectric nanogenerator for harnessing the mechanical energy from the human body. Firstly, a PVDF based nanogenerator is fabricated, and then to enhance its output performance rGO and boron doped rGO are added in polymer matrix. Then output performance of all the fabricated PNG are compared which shows that incorporation of conducting nanofillers in PVDF matrix improves the output performance. A maximum open-circuit voltage, short-circuit current and power density of 13.8 V, 5.5 μA and ~ 42.3 $\mu W/cm^2$ is obtained for PVDF/boron doped rGO (PBR) nanocomposite film based piezoelectric nanogenerator. To demonstrate the PNG's practical applicability, energy produced by PNG is stored in 1μF capacitor and utilized to power LEDs connected in series. Finally, the fabricated device is demonstrated to harness energy from daily life activities of human body such as wrist bending, leg folding, foot tapping and elbow bending.

2 Synthesis and experimental details

The rGO is synthesized by our previous reported paper using hydrothermal approach [22]. For the synthesis of boron doped rGO, 1 g of boric acid is mixed into an aqueous solution of GO and sonicated for 30 min for homogeneous dispersion. The prepared

solution is then transferred to Teflon lined autoclave and kept in oven at 180 °C for 12 h. After being washed multiple times with DI water and ethanol, the resulting product is kept in an oven overnight at 60 °C for drying to get nanosheets of boron doped rGO (B-rGO). Subsequently, a simple drop casting method is used for synthesis of the PVDF and PVDF nanocomposite films. First, 1 g of PVDF is mixed in 10 ml *N,N*-dimethylformamide (DMF) with the help of magnetic stirrer until PVDF powder is completely dissolved in the solvent to obtain transparent solution. Then 10 mg of B-rGO is added to the above solution and stir for 45 min. After that the resultant solution is drop casted on clean glass substrate with the help of micropipette and placed in oven for 2 h at 90 °C to remove any solvent. Then after natural cool down, the films are dipped in DI water to obtain freestanding films. The rGO doped film is also prepared by the same procedure by adding 10 mg of rGO in the PVDF/DMF solution.

2.1 Fabrication of the piezoelectric nanogenerator

To fabricate PNG, first the PVDF and PVDF composite films are cut into the requisite shape and aluminum electrode of thickness 100 nm is deposited on both sides of film of area 2×2 cm^2 with thermal evaporation technique. After that two copper wires are drawn from the top and bottom aluminum electrode surface for the external connection and finally the entire device is encapsulated with Kapton tape. The detailed schematic diagram showing the fabrication of piezoelectric nanogenerator has already been published by our group [22].

3 Characterization techniques

Firstly, synthesized powder samples of rGO and B-rGO are characterized by X-ray diffractometer and Raman spectroscopy technique using Rigaku, Ultima diffractometer and WiTec alpha 300 RA model with a laser source of 532 nm wavelength. X-ray photoelectron spectroscopy (XPS) measurements are recorded by Nexsa base spectrometer with Aluminium K$_\alpha$ source for chemical composition analysis. The surface morphologies of the samples together with the energy-dispersive X-ray spectroscopy (EDS) are observed under a field emission scanning electron microscopy

via Nova Nano SEM. Fourier transform infrared spectroscopy (FTIR) spectra of the polymer composite films are obtained by Perkin Elmer Spectrum II spectrometer. The Marine India PE loop tracer is used to measure polarization versus electric field (P–E) loops and YE2730A d$_{33}$ meter is used to measure the piezoelectric coefficient (d$_{33}$) of PVDF and PVDF composite films. The crystallinity of the films are measured using Differential Scanning calorimeter (DSC 8000, Perkin Elmer). Finally, in order to measure output performance of PNG, the V$_{OC}$ and I$_{SC}$ measurements are carried out by Tektronix MDO500 oscilloscope and Keithley DMM7510 digital multimeter.

4 Results and discussion

Figure 1a shows the XRD pattern of synthesized rGO and B-rGO samples. Both the samples show the diffraction peak corresponding to (002) plane which is characteristic peak of graphitic materials. For rGO, the peak corresponding to (002) plane is appeared at $2\theta = 24.84°$, whereas in B-rGO case the peak is shifted right and appear at 25.14°. The corresponding value of interlayer spacing for rGO and B-rGO is 3.58 Å and 3.53 Å respectively. The decrease in the interlayer spacing can be attributed due to the fact that when we dope boron atom in rGO matrix, it gives rise to strain because of the different atomic size of boron and carbon atom resulting in peak shift [29, 30]. Also, the reduction of π electron density between graphene planes may be the another possible reason for low interlayer spacing in B-rGO due to the replacement of carbon by boron atom [31].

As we know, the crystallinity and homogeneity of the rGO and heteroatom doped rGO is highly sensitive to the synthesis route. Therefore, to evaluate the degree of disorder within the carbon samples, Raman analysis for the rGO and B-rGO are collected at an excitation wavelength of 532 nm. The Raman spectra of all samples exhibit two major Raman peaks at 1344 and 1586 cm^{-1} corresponds to the D and G band and a wide 2D-band around 2800 cm^{-1} corresponding to the carbon structure in rGO as depicted in Fig. 1b. In the Raman spectra, D band stems from the structural defects and disorder structure in graphitic lattice while G bands ascribed to inplane stretching of C=C bonds and first order E$_{2g}$ optical mode of graphite. To further deduce the degree of disorder and defects present in rGO sample after doping, I$_D$/I$_G$ ratio of

Fig. 1 a XRD and **b** Raman spectra of synthesized rGO and B-rGO samples
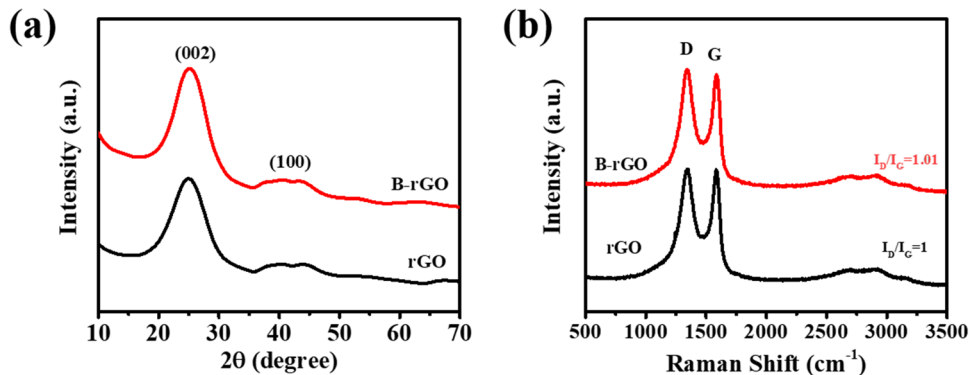

the rGO and B-rGO is calculated which shows that when we dope the boron atom in rGO, the I_D/I_G ratio increases slightly from 1 to 1.01. This slight increment in the value of I_D/I_G ratio shows the successful doping of boron atom and increased amount of disorder in sp^2 domains and structural defects in B-rGO [32, 33].

To further support the successful incorporation of boron atom in rGO, the X-ray photoelectron spectroscopy (XPS) analysis is carried out for rGO and B-rGO samples where in the survey spectrum, rGO has only C1s (285.2 eV) and O1s (532.9 eV) peaks, whereas for B-rGO an additional B1s (192.7 eV) peak is observed

showing that boron atoms are bonded to rGO network (Fig. 2a). Figure 2b shows the high resolution deconvoluted C1s spectra of rGO which is divided into four peaks at different binding energy levels (284.5, 285.4, 288.2, and 290.6 eV). The peak at 284.5 eV corresponds to sp^2 hybridized C–C bond, while the peaks at 285.4, 288.2, and 290.6 eV corresponds to C–O, C=O and O–C=O bonds respectively [22, 29, 34]. Figure 2c shows the high resolution C1s spectra of B-rGO, where B-rGO sample have all the functional groups as that in case of rGO with the exception that peak at 290.6 eV is shifted to 290.1 eV and this new peak corresponds to

Fig. 2 a XPS survey spectra of rGO and B-rGO, High resolution deconvoluted C1s spectra of **b** rGO and **c** B-rGO, **d** B1s spectra of B-rGO
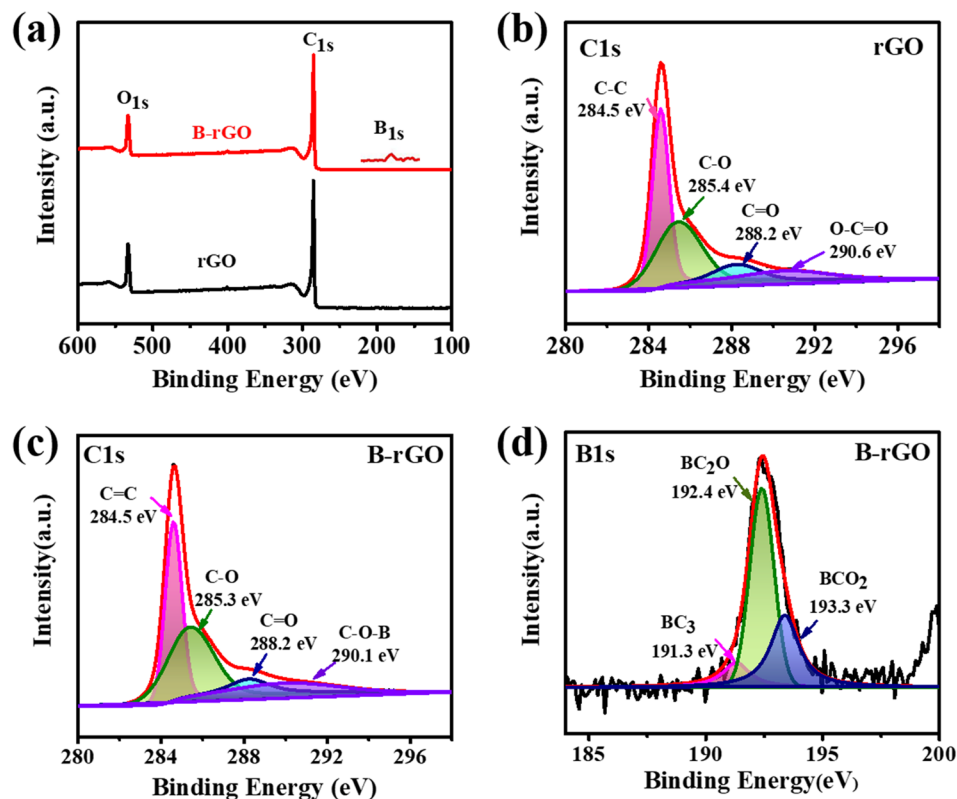
the C–O–B bond. Figure 2d shows the high resolution B1s spectra of B-rGO, which is deconvoluted in three peaks at binding energies 191.3, 192.4 and 193.3 eV corresponding to BC_3, BC_2O and BCO_2 bond respectively [26, 35]. The B1s spectra of B-rGO demonstrates that boron can exist in three different form, first is by substitution of carbon atom by boron atom in the rGO network to form bond BC_3, second is co-doping with the oxygen to form BC_2O bond which creates nanovoids in layer and third is BCO_2 bond resulting from the formation of functional groups [36]. These results not only confirm the successful incorporation of boron atoms in rGO network but also show that the interlayer spacing increases and more defects are introduced in rGO network.

For structural and morphological analysis, FESEM micrographs are obtained for rGO and boron doped rGO samples. As depicted in Fig. 3a–b, rGO exhibit of randomly aggregated layered structure where few layer of sheets that are closely associated with one another and after doping of boron atom in rGO the aggregation increases. In addition, Energy Dispersive X-ray spectroscopy (EDX) analysis have also been carried out on B-rGO for the elemental analysis of the sample. The EDX spectra confirms the presence of C, O, and B elements for B-rGO sample is illustrated in Fig. 3c–f that further confirm the presence of boron atom in rGO network. After successful synthesis of rGO and B-rGO samples, they are mixed in PVDF and DMF solution to fabricate the polymer composite films. The samples of pure PVDF, rGO doped PVDF and B-rGO doped PVDF are described as P, PR and PBR respectively.

To confirm the existence of different phases in pristine PVDF and PVDF composite films, XRD and FTIR analysis is carried out. Figure 4a depicts the

Fig. 3 Morphological characterization of the synthesized **a** rGO and **b** B-rGO powder sample. **c** EDX spectra and **d** elemental mapping of C, O, and B atom present in the B-rGO sample
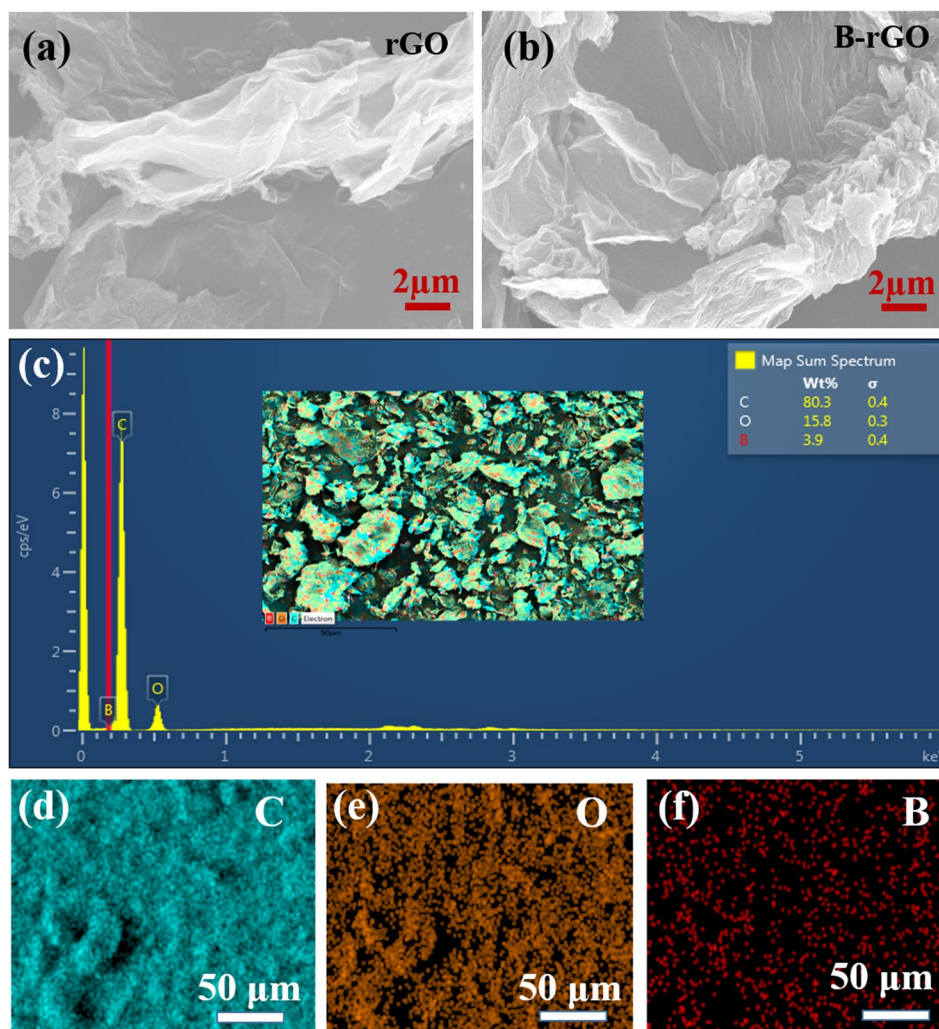
XRD pattern of P, PR and PBR composite films where all the samples exhibit two characteristic peak. The presence of a small characteristic peak at ~ 18.4° correspond to (100) plane belongs to the non-polar α phase, whereas the presence of sharp intense peak at ~ 20.4° corresponds to (200) plane of polar β phase of the PVDF [37, 38]. It can be clearly seen from the graph, that the intensity of peak at ~ 20.4° grows, which proves enhanced polar phase in PVDF with addition of rGO and B-rGO as a nanofillers materials. Moreover, to further investigate the crystal phases of PVDF, FTIR analysis is carried out on the synthesized polymer and polymer composite films. Figure 4b shows the FTIR spectra of pristine PVDF and

PVDF composite films, where peaks at 612, 764, 795, and 1382 cm^{-1} are attributed to non-polar α phase with trans-gauche-trans-gauche (TGTG) conformation, whereas the peaks at 840 cm^{-1} and 1275 cm^{-1} are related to electroactive polar β phase of PVDF and arises due to the asymmetrical stretching of –CF$_2$ and oscillating vibration of –CH$_2$ dipoles [39, 40]. In comparison to pristine PVDF film, the intensity of absorbance peaks corresponding to α phase is decreasing in PR and PBR films indicating that when rGO and B-rGO are doped in PVDF matrix, they aid in the formation of crystalline phase. The relative content of the polar phases in PVDF is calculated with the help of Lambert-Beer law using absorption
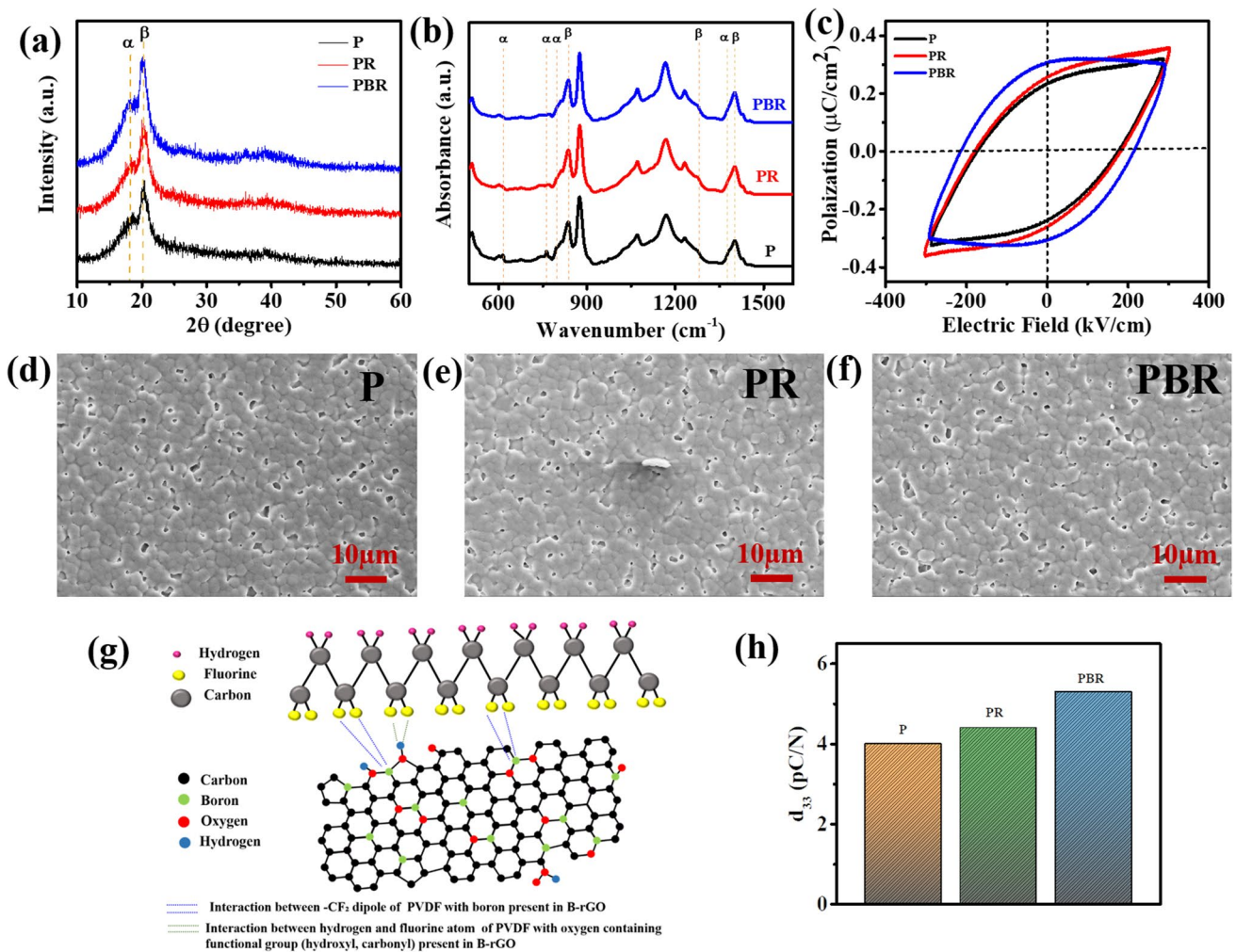

Fig. 4 **a–c** XRD, FTIR and P–E loops of the pure PVDF (P), PVDF/rGO (PR) and PVDF/B-rGO films, respectively, **d–f** FESEM images showing the morphology of P, PR and PBR films, **g** A schematic representation showing the interaction between dipoles present in PVDF and the filed B-rGO in the PVDF matrix, **h** piezoelectric strain coefficient d$_{33}$ of P, PR and PBR films

bands at 761 cm^{-1} and 840 cm^{-1} and is given by the equation.

$$F(\beta) = \frac{A_\beta}{\left(\frac{k_\beta}{k_\alpha}\right)A_\alpha + A_\beta} \times 100\%,$$

where, A_α and A_β are the absorbance of α and β phase at 761 cm^{-1} and 840 cm^{-1} and k_α and k_β are the absorption coeffecient at respective wavenmber ($k_\alpha = 6.1 \times 10^4$ cm^2 mol^{-1}, $k_\beta = 7.7 \times 10^4$ cm^2 mol^{-1}) and $F(\beta)$ represents the relative fraction of β phase [41]. The value of $F(\beta)$ obtained for pristine PVDF is ~ 69% and after loading the rGO and B-rGO the value of $F(\beta)$ becomes ~ 77% and ~ 80% respectively. The substantially increased value of $F(\beta)$ can be understood by the fact that when we add rGO and B-rGO in the PVDF matrix, there is strong interaction between the surface charges arise due to decolalized π electron, boron atom and oxygen containing functional group in rGO and B-rGO with the –CH$_2$ and –CF$_2$ dipoles of the polymer chain [21, 42]. The fluorine group of PVDF interacts with boron and oxygen containg functional groups present on basal plane of B-rGO, allowing PVDF chain to crystallize on their surface in trans-trans-trans-trans(TTTT) conformation, faciliating the tranformation of non-polar α phase to the polar β phase. The proposed mechanism for the formation of electroactive polar phase after doping is shown in Fig. 4g. Thus, it can be concluded that the addition of rGO and B-rGO acts as a nucleating agent, which helps in inducing electroactive polar phase in PVDF segment by rotating the polymer chain in all trans configuration. Furthermore, to verify the enhanced piezoelectric properties of the composite films, a comparison between the polarization versus electric field (P–E) hysteresis loop analysis is done on the films to reveal the effect of rGO and B-rGO doping on the ferroelectricity of nanocomposite films. The P–E loops show that after incorporating rGO and B-rGO in PVDF matrix, the ferroelectric properties of polymer film improve. The value of remnant polarization which indicates the internal dipole moment per unit volume when applied electric field is zero obtained from the P–E loops are 0.23, 0.26 and 0.31 μC/cm^2 for P, PR and PBR films respectively as shown in Fig. 4c. The improved value of remnant polarization after addition of rGO and B-rGO illustrate that addition nanofillers helps in alignment of dipole in the PVDF film and a maximum value of the remnant polarization corresponds to PBR composite film. In order to further confirm the enhancement in the piezoelectric properties of PVDF after doping of rGO and B-rGO, the piezoelectric strain coefficient d$_{33}$ is measured with the help of Sino Cera YE2730 d$_{33}$ meter, which relates the electric field produced for an applied electric stress. The value of d$_{33}$ for P, PR and PBR films are 4, 4.4 and 5.3 pC/N respectively as shown in Fig. 4h. The increase in the value of d$_{33}$ in the composite is attributed due to increase in interfacial polarization after addition of the rGO and B-rGO in the PVDF matrix which is in agreement with P–E and FTIR studies. The effect of addition of rGO and B-rGO on the crystallization and melting temperature of PVDF composite films were analyzed by DSC as the piezoelectric behavior of the nanocomposite films are dependent on the crystalline structure as well as the stability of the electroactive polar phase of the nanocomposite films [43]. Figure 5a–b shows the DSC thermographs of pristine PVDF and PVDF nanocomposite films, which shows that when we add nanofillers in PVDF matrix, the melting temperature (T$_m$), melting enthalpy (ΔH$_m$), and crystalline temperature (T$_c$) increases gradually as shown in Table 1. The shifting of peak towards high temperature is attributed to the transformation from α phase to β phase which is

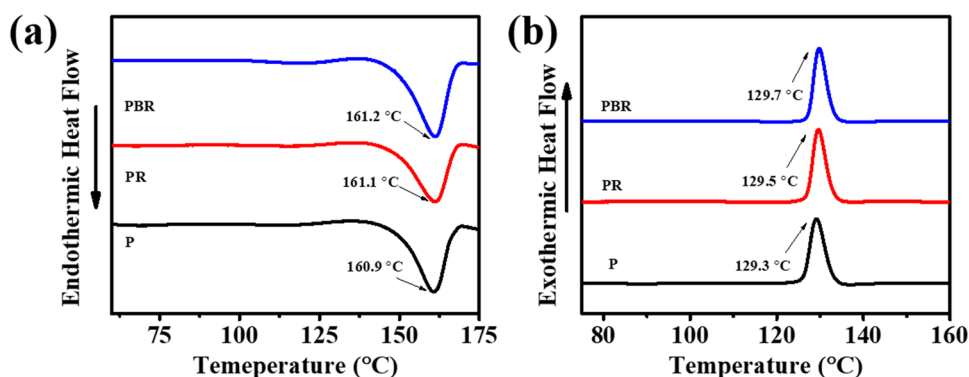**Fig. 5** DSC **a** heating and **b** cooling curves of PVDF and PVDF nanocomposite films

Table 1 The DSC parameters of pristine PVDF and PVDF nanocomposite films

| Sample	T_m (°C)	T_c (°C)	ΔH_m	χ_c(%)
P	160.9	129.3	28.73	27.49
PR	161.1	129.5	31.25	30.21
PBR	161.2	129.7	33.27	32.16

in accordance with XRD and FTIR studies [44]. The percentage crystallinity is determined by the following equation.

$$\chi_c(\%) = \frac{\Delta H_m}{(1-\varphi)\Delta H_m^{\circ}} \times 100\%,$$

where, ΔH_m is melting enthalpy, ϕ is filler loading percentage, and ΔH_m° is the melting enthalphy of 100% crystalline PVDF (i.e. 104.5 J/g). The calculated value of χ_c for pristine PVDF and PVDF nanocomposite films are shown in Table 1. The percentage crystallinity also increase from ~ 27% in pristine PVDF film to ~ 32% in PBR film. Furthermore, to check the surface morphology of the polymer and polymer composite films, FESEM images are taken for the PVDF and PVDF nanocomposite films (Fig. 4d–f) which shows that rGO and B-rGO nanosheets are evenly distributed in the PVDF polymer matrix without aggregation.

The PNG structure with the corresponding working principle is illustrated in Fig. 6. In initial state, when no force is imparted on device (Fig. 6a), PNG does not deliver any electrical output due to presence of the existing unpolarized electric dipoles in the film. Therefore, when we start to apply force on device (Fig. 6b), film starts deforming to polarize the electric dipoles inside the film and due to polarization effect, electric charges are induced on both electrodes, causing charges to flow from bottom to top electrode. When force is removed (Fig. 6c) the compressive stress fades away in the film leading the electron to flow in the opposite direction until PNG device returns to its initial state. This periodic process results in generation of positive and negative potential cycles in output of nanogenerator.

The piezoelectric energy harvesting performance of PNG device is analyzed by periodic tapping of nanogenerator with the help of the dynamic shaker and measuring the corresponding open-circuit
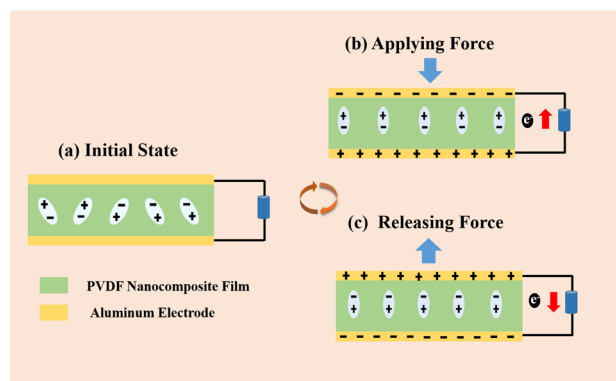
Fig. 6 A schematic showing the working mechanism of piezoelectric nanogenerator

voltage (V_{OC}) and short-circuit (I_{SC}) current with the help of the oscilloscope and digital multimeter. In our previous study, we have demonstrated that when we tap the nanogenerator at different frequency, maximum voltage is obtained corresponding to 6 Hz tapping frequency. Therefore, in this paper we have measured the open-circuit voltage and short-circuit current of P, PR, and PBR films at 6 Hz frequency only. Figure 7a–c depicts the measured open-circuit voltage of the fabricated PNG, in which maximum voltage of 13.8 V is produced by PBR film based PNG, whereas pristine PVDF and PR film based PNG produce an output voltage of 7.6 and 12.2 V respectively. The value of rectified short-circuit current obtained for P, PR and PBR film based PNG are 2.6 μA, 4.72 μA and 5.57 μA respectively (Fig. 7d–f). Furthermore, the effect of tapping frequency on the output voltage of PBR film based PNG is also examined which also further verify that maximum output voltage corresponds to the 6 Hz frequency as shown in Fig. 8a. Among all the fabricated device, PNG made by PBR film show maximum output in comparison to PVDF and PR film based PNG. The enhanced performance of PBR film based PNG can be ascribed due to the following aspects. First, adding boron doped rGO in PVDF helps in nucleation of β phase which is supported by XRD, FTIR and P–E studies. Second, it has been reported in the literature that selective surface adsorption of atoms in graphene can induce the piezoelectricity in it by breaking the inversion symmetry, therefore it is possible that when we add boron atom in rGO it will break the inversion symmetry and induce piezoelectricity in it [45]. Third, rGO is conducting in nature
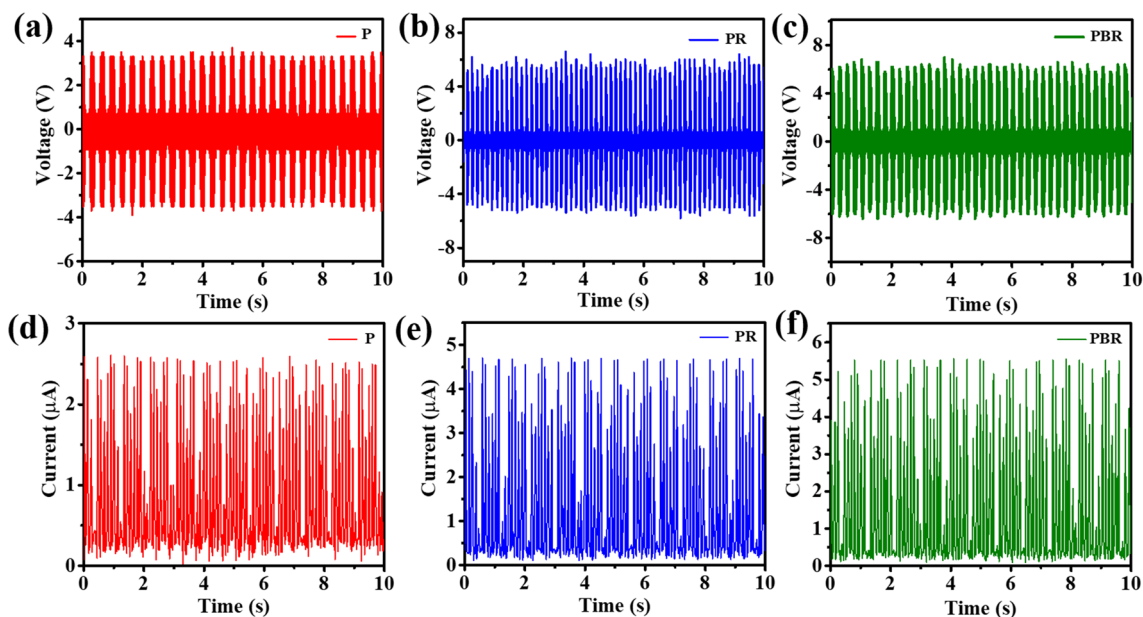
Fig. 7 a–c Open-circuit voltage and **d–f** rectified short-circuit current measurements of P, PR, and PBR film based PNG device
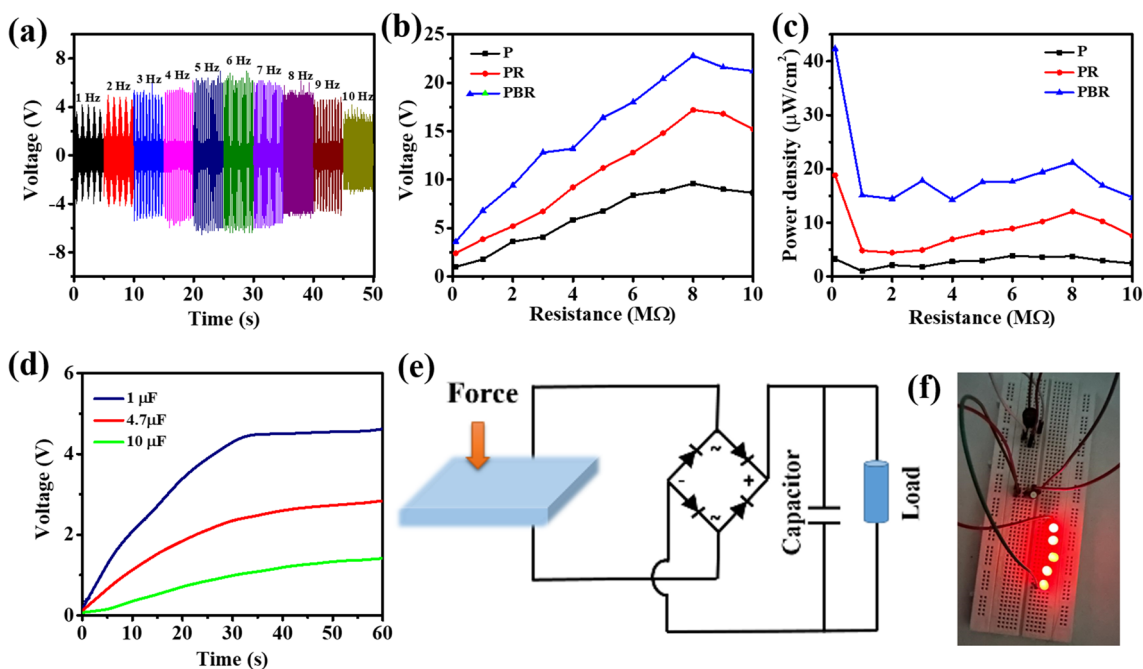

Fig. 8 a The measured output voltage of PBR film based PNG as a function of frequency. **b** Variation of output voltage and **c** power density as a function of load resistance, **d** Charging of 1, 4.7, and 10 μF capacitor by the generated voltage of PBR based device, **e** A circuit diagram for storing the energy generated by PNG in the capacitor to power up LEDs **f** digital photograph showing LEDs powered by PNG

therefore when we add it in the polymer matrix it forms conducting channels which helps in the better charge transfer as a result increase the output performance of the PBR film based PNG device [46].

The variation of the output voltage of P, PR PBR film based PNG devices across the varied load resistance are shown in Fig. 8b, where maximum voltage is corresponding to 8 MΩ resistance after that voltage

first saturates and then start decreasing. Figure 8c depicts the power density curves of the corresponding films, with a maximum power density of ~ 42.3 $\mu W/cm^2$ is attained for PBR based PNG device. As the output of the PNG is AC in nature, therefore to store the generated energy a bridge rectifier is utilized to convert AC voltage to DC voltage. Figure 8d shows the energy generated by PBR film based PNG device and is stored in different capacitors (1, 4.7 and 10 μF). It is clearly seen from the graph that 1

μF capacitor can charge upto ~ 4.6 V in 60 s while 4.7 and 10 μF capacitor can charge upto 2.8 V and 1.4 V respectively. The stored energy is then further used to light up different LEDs and their corresponding circuit design is shown in Fig. 8e. The PBR film based PNG device can light up maximum 5 LEDs with the digital picture illustrated in Fig. 8f and corresponding video is placed in supplementary. Furthermore, the as fabricated nanogenerator is utilized to harness biomechanical energy from human body
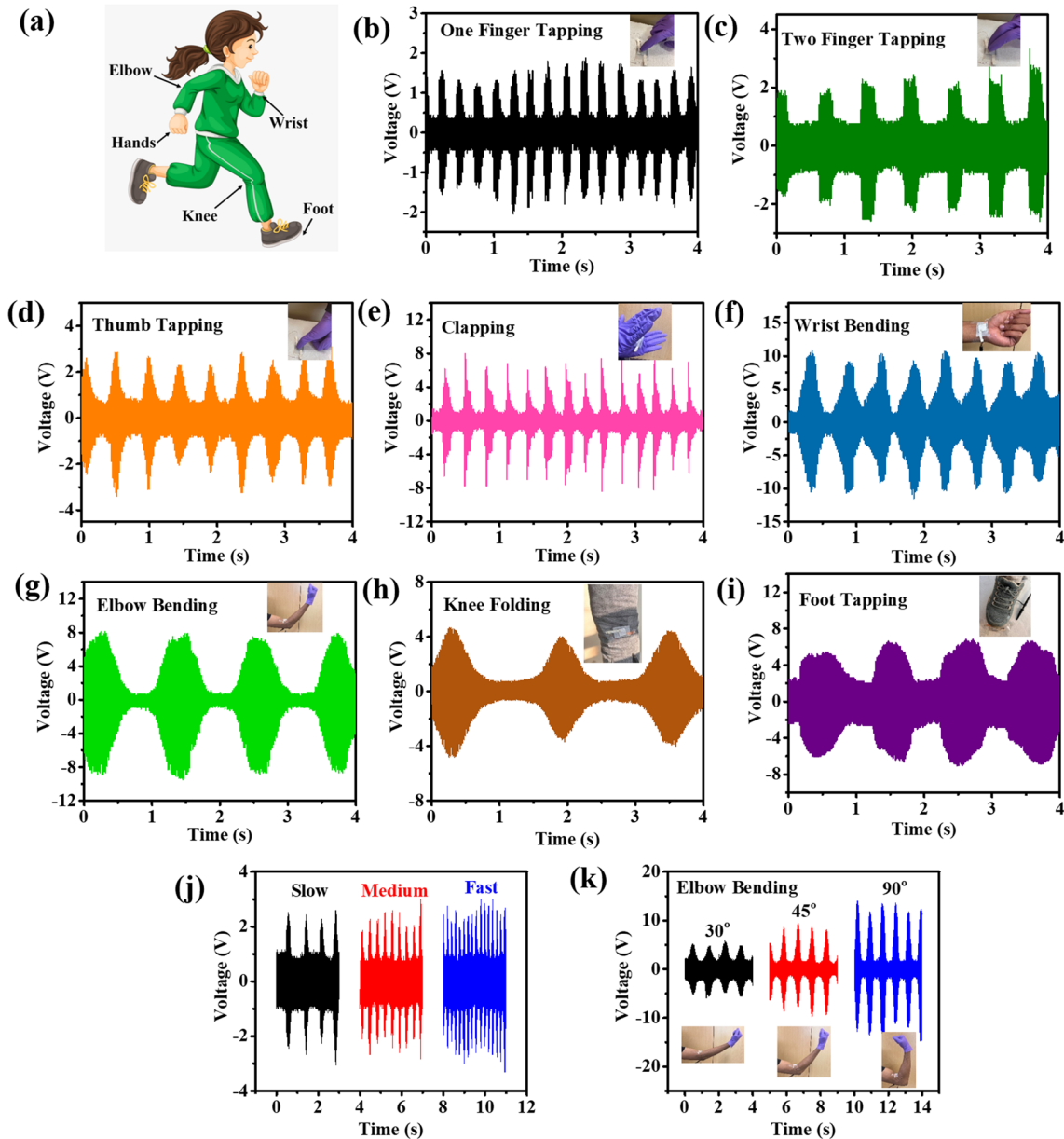

Fig. 9 a A schematic representation of different parts of human body from which energy can be harvested. The output voltage generated by PBR film based PNG by **b** one finger, **c** two fingers, **d** thumb tapping, **e** clapping, **f** wrist bending, **g** elbow bending, **h** knee folding, and **i** foot tapping, **j** variation in the output performance of PNG by slow, moderate and fast finger tapping, **k** The voltage produced by PNG by bending elbow at different angles

by attaching it to different parts of the body and a schematic representation of human body parts from which energy has been harvested is shown in Fig. 9a. Figure 9b–d illustrates the output voltage generated by PNG by tapping it with one finger, two finger and thumb. The variation of the tapping with finger in slow, moderate and high speed is also illustrated in Fig. 9j. The output voltage generated by nanogenerator by clapping and attaching it to wrist, elbow, knee, and tapping it with foot are illustrated in Fig. 9e–i. We also measured PNG's output voltage by bending elbow at various angles (30°, 45° and 90°) as illustrated in Fig. 9k. The above results demonstrate the flexible PBR film based PNG is an effective device that can harness biomechanical energy from the human motion. Thus, by harvesting the energy associated with these various biomechanical motions, it is possible to design a pervasive, sustainable and environmental friendly energy solution for the bioelectronics which will revolutionize the future of wearable electronics in upcoming era of IoT and artificial intelligence [47–49].

5 Conclusion

In this work, rGO and B-rGO are successfully synthesized by the hydrothermal technique and are incorporated in the PVDF matrix to synthesize polymer nanocomposite films. It is realized that incorporating rGO and B-rGO into the PVDF matrix improves device piezoresponse by increasing nucleation, which improves content of β phase in PVDF nanocomposite film. A maximum open-circuit voltage and short-circuit current of 13.8 V and 5.5 μA is produced by the boron doped rGO/PVDF film based device whereas pristine PVDF based PNG can only generate an output voltage and current of 7.6 V and 2.6 μA, respectively by tapping the nanogenerator with 6 Hz frequency. The practical applicability of the as fabricated nanogenerator is demonstrated by storing the harvested energy in the capacitor which is used to power up 5 LEDs connected in series. The fabricated PNG also demonstrated energy harvesting from the human movements, which includes finger tapping, foot tapping, elbow bending, wrist movements and leg folding. Hence, the current study proposes an effective strategy of using biocompatible PVDF flexible films for harvesting the various biomechanical energy for biomedical sector such

as drug delivery, cell stimulation, body patchable device, sensors, and so on, paving a new path for designing a self-powered system by providing a pervasive energy solution for smart and versatile wearable bioelectronics devices.

Author contributions

SR: conceptualization, data curation, methadology, fabrication, writing original draft. BS: supervision, writing review & editing.

Data availability

The data will be made available on reasonable request.

Declarations

Conflict of interest The authors declare that there is no conflicts of interest.

Supplementary information The online version contains supplementary material available at https://doi.org/10.1007/s10854-023-11207-x.

References

1. M. Zhou, M.S.H. Al-Furjan, J. Zou, W. Liu, A review on heat and mechanical energy harvesting from human—Principles, prototypes and perspectives. Renew. Sustain. Energy Rev. **82**, 3582–3609 (2018). https://doi.org/10.1016/j.rser.2017.10.102
2. F. Mokhtari, Z. Cheng, R. Raad, J. Xi, J. Foroughi, Piezofibers to smart textiles: a review on recent advances and future outlook for wearable technology. J. Mater. Chem.

A **8**, 9496–9522 (2020). https://doi.org/10.1039/D0TA00227E

3. S. Li, J. Wang, W. Peng, L. Lin, Y. Zi, S. Wang, G. Zhang, Z.L. Wang, Sustainable energy source for wearable electronics based on multilayer elastomeric triboelectric nanogenerators. Adv. Energy Mater. **7**, 1602832 (2017). https://doi.org/10.1002/aenm.201602832

4. X. Chen, Y. Song, Z. Su, H. Chen, X. Cheng, J. Zhang, M. Han, H. Zhang, Flexible fiber-based hybrid nanogenerator for biomechanical energy harvesting and physiological monitoring. Nano Energy **38**, 43–50 (2017). https://doi.org/10.1016/j.nanoen.2017.05.047

5. Q. Zhang, Q. Liang, D.K. Nandakumar, H. Qu, Q. Shi, F.I. Alzakia, D.J.J. Tay, L. Yang, X. Zhang, L. Suresh, Shadow enhanced self-charging power system for wave and solar energy harvesting from the ocean. Nat. Commun. **12**, 616 (2021). https://doi.org/10.1038/s41467-021-20919-9

6. S. Wu, T. Li, Z. Tong, J. Chao, T. Zhai, J. Xu, T. Yan, M. Wu, Z. Xu, H. Bao, High-performance thermally conductive phase change composites by large-size oriented graphite sheets for scalable thermal energy harvesting. Adv. Mater. **31**, 1905099 (2019). https://doi.org/10.1002/adma.201905099

7. J. Wang, S. Zhou, Z. Zhang, D. Yurchenko, High-performance piezoelectric wind energy harvester with Y-shaped attachments. Energy. Convers. Manag. **181**, 645–652 (2019). https://doi.org/10.1016/j.enconman.2018.12.034

8. M. Liu, F. Qian, J. Mi, L. Zuo, Biomechanical energy harvesting for wearable and mobile devices: state-of-the-art and future directions. Appl. Energy **321**, 119379 (2022). https://doi.org/10.1016/j.apenergy.2022.119379

9. B. Dudem, D.H. Kim, L.K. Bharat, J.S. Yu, Highly-flexible piezoelectric nanogenerators with silver nanowires and barium titanate embedded composite films for mechanical energy harvesting. Appl. Energy **230**, 865–874 (2018). https://doi.org/10.1016/j.apenergy.2018.09.009

10. S. Siddiqui, H.B. Lee, D.I. Kim, L.T. Duy, A. Hanif, N.E. Lee, An omnidirectionally stretchable piezoelectric nanogenerator based on hybrid nanofibers and carbon electrodes for multimodal straining and human kinematics energy harvesting. Adv. Energy Mater. **8**, 1701520 (2018). https://doi.org/10.1002/aenm.201701520

11. P. Yingyong, P. Thainiramit, S. Jayasvasti, N. Thanach-Issarasak, D. Isarakorn, Evaluation of harvesting energy from pedestrians using piezoelectric floor tile energy harvester. Sens. Actuators A **331**, 113035 (2021). https://doi.org/10.1016/j.sna.2021.113035

12. Z. Liu, S. Zhang, Y. Jin, H. Ouyang, Y. Zou, X. Wang, L. Xie, Z. Li, Flexible piezoelectric nanogenerator in wearable self-powered active sensor for respiration and healthcare monitoring. Semicond. Sci. Technol. **32**, 064004 (2017). https://doi.org/10.1088/1361-6641/aa68d1

13. S.H. Wankhade, S. Tiwari, A. Gaur, P. Maiti, PVDF—PZT nanohybrid based nanogenerator for energy harvesting applications. Energy Rep. **6**, 358–364 (2020). https://doi.org/10.1016/j.egyr.2020.02.003

14. Z.L. Wang, J. Song, Piezoelectric nanogenerators based on zinc oxide nanowire arrays. Science **312**, 242–246 (2006). https://doi.org/10.1126/science.1124005

15. H. Su, X. Wang, C. Li, Z. Wang, Y. Wu, J. Zhang, Y. Zhang, C. Zhao, J. Wu, H. Zheng, Enhanced energy harvesting ability of polydimethylsiloxane-BaTiO3-based flexible piezoelectric nanogenerator for tactile imitation application. Nano Energy **83**, 105809 (2021). https://doi.org/10.1016/j.nanoen.2021.105809

16. L. Lu, W. Ding, J. Liu, B. Yang, Flexible PVDF based piezoelectric nanogenerators. Nano Energy **78**, 105251 (2020). https://doi.org/10.1016/j.nanoen.2020.105251

17. M.A. Johar, J.-H. Kang, M.A. Hassan, S.-W. Ryu, A scalable, flexible and transparent GaN based heterojunction piezoelectric nanogenerator for bending, air-flow and vibration energy harvesting. Appl. Energy **222**, 781–789 (2018). https://doi.org/10.1016/j.apenergy.2018.04.038

18. S. Badatya, D.K. Bharti, N. Sathish, A.K. Srivastava, M.K. Gupta, Humidity sustainable hydrophobic poly (vinylidene fluoride)-carbon nanotubes foam based piezoelectric nanogenerator. ACS Appl. Mater. Interfaces **13**, 27245–27254 (2021). https://doi.org/10.1021/acsami.1c02237

19. A. Anand, D. Meena, K.K. Dey, M.C. Bhatnagar, Enhanced piezoelectricity properties of reduced graphene oxide (RGO) loaded polyvinylidene fluoride (PVDF) nanocomposite films for nanogenerator application. J. Polym. Res. **27**, 1–11 (2020). https://doi.org/10.1007/s10965-020-02323-x

20. X. Hu, Z. Ding, L. Fei, Y. Xiang, Y. Lin, Wearable piezoelectric nanogenerators based on reduced graphene oxide and in situ polarization-enhanced PVDF-TrFE films. J. Mater. Sci. **54**, 6401–6409 (2019). https://doi.org/10.1007/s10853-019-03339-5

21. S.K. Karan, D. Mandal, B.B. Khatua, Self-powered flexible Fe-doped RGO/PVDF nanocomposite: an excellent material for a piezoelectric energy harvester. Nanoscale **7**, 10655–10666 (2015). https://doi.org/10.1039/C5NR02067K

22. S. Rana, V. Singh, B. Singh, Tailoring the output performance of PVDF-based piezo–tribo hybridized nanogenerators via B, N-codoped reduced graphene oxide. ACS Appl. Electron. Mater. **4**, 5893–5904 (2022). https://doi.org/10.1021/acsaelm.2c01085

23. J.-H. Ji, B.S. Kim, J. Kang, J.-H. Koh, Improved output performance of hybrid composite films with nitrogen-doped reduced graphene oxide. Ceram. Int. (2021). https://doi.org/10.1016/j.ceramint.2021.12.271

24. S. Li, Z. Wang, H. Jiang, L. Zhang, J. Ren, M. Zheng, L. Dong, L. Sun, Plasma-induced highly efficient synthesis of boron doped reduced graphene oxide for supercapacitors. Chem. Commun. **52**, 10988–10991 (2016). https://doi.org/10.1039/C6CC04052G

25. N. Venkatesan, K.S. Archana, S. Suresh, R. Aswathy, M. Ulaganthan, P. Periasamy, P. Ragupathy, Boron-doped graphene as efficient electrocatalyst for zinc–bromine redox flow batteries. ChemElectroChem **6**, 1107–1114 (2019). https://doi.org/10.1002/celc.201801465

26. H. Fang, C. Yu, T. Ma, J. Qiu, Boron-doped graphene as a high-efficiency counter electrode for dye-sensitized solar cells. Chem. Commun. **50**, 3328–3330 (2014). https://doi.org/10.1039/C3CC48258H

27. Z. Fan, Y. Li, X. Li, L. Fan, S. Zhou, D. Fang, S. Yang, Surrounding media sensitive photoluminescence of boron-doped graphene quantum dots for highly fluorescent dyed crystals, chemical sensing and bioimaging. Carbon **70**, 149–156 (2014). https://doi.org/10.1016/j.carbon.2013.12.085

28. R.S. Sahu, K. Bindumadhavan, R. Doong, Boron-doped reduced graphene oxide-based bimetallic Ni/Fe nanohybrids for the rapid dechlorination of trichloroethylene. Environ. Sci. **4**, 565–576 (2017). https://doi.org/10.1039/C6EN00575F

29. R.N. Muthu, S.S.V. Tatiparti, Electrode and symmetric supercapacitor device performance of boron-incorporated reduced graphene oxide synthesized by electrochemical exfoliation. Energy Storage **2**, e134 (2020). https://doi.org/10.1002/est2.134

30. L.K. Putri, B.-J. Ng, W.-J. Ong, H.W. Lee, W.S. Chang, S.-P. Chai, Heteroatom nitrogen-and boron-doping as a facile strategy to improve photocatalytic activity of standalone reduced graphene oxide in hydrogen evolution. ACS Appl. Mater. Interfaces **9**, 4558–4569 (2017). https://doi.org/10.1021/acsami.6b12060

31. M. Endo, C. Kim, T. Karaki, T. Tamaki, Y. Nishimura, M.J. Matthews, S.D.M. Brown, M.S. Dresselhaus, Structural analysis of the B-doped mesophase pitch-based graphite fibers by Raman spectroscopy. Phys. Rev. B **58**, 8991 (1998). https://doi.org/10.1103/PhysRevB.58.8991

32. Y. Hishiyama, H. Irumano, Y. Kaburagi, Y. Soneda, Structure, Raman scattering, and transport properties of boron-doped graphite. Phys. Rev. B **63**, 245406 (2001)

33. J. Li, X. Li, D. Xiong, L. Wang, D. Li, Enhanced capacitance of boron-doped graphene aerogels for aqueous symmetric supercapacitors. Appl. Surf. Sci. **475**, 285–293 (2019). https://doi.org/10.1016/j.apsusc.2018.12.152

34. T. Zhu, S. Li, B. Ren, L. Zhang, L. Dong, L. Tan, Plasma-induced synthesis of boron and nitrogen co-doped reduced graphene oxide for super-capacitors. J. Mater. Sci. **54**, 9632–9642 (2019)

35. W. Cheng, X. Liu, N. Li, J. Han, S. Li, S. Yu, Boron-doped graphene as a metal-free catalyst for gas-phase oxidation of benzyl alcohol to benzaldehyde. RSC Adv. **8**, 11222–11229 (2018). https://doi.org/10.1039/C8RA00290H

36. Y. Wang, C. Wang, Y. Wang, H. Liu, Z. Huang, Boric acid assisted reduction of graphene oxide: a promising material for sodium-ion batteries. ACS Appl. Mater. Interfaces **8**, 18860–18866 (2016). https://doi.org/10.1021/acsami.6b04774

37. V. Singh, D. Meena, H. Sharma, A. Trivedi, B. Singh, Investigating the role of chalcogen atom in the piezoelectric performance of PVDF/TMDCs based flexible nanogenerator. Energy **239**, 122125 (2022). https://doi.org/10.1016/j.energy.2021.122125

38. B. Jaleh, A. Jabbari, Evaluation of reduced graphene oxide/ZnO effect on properties of PVDF nanocomposite films. Appl. Surf. Sci. **320**, 339–347 (2014). https://doi.org/10.1016/j.apsusc.2014.09.030

39. X. Cai, T. Lei, D. Sun, L. Lin, A critical analysis of the α, β and γ phases in poly (vinylidene fluoride) using FTIR. RSC Adv. **7**, 15382–15389 (2017). https://doi.org/10.1039/C7RA01267E

40. F. Wang, H. Sun, H. Guo, H. Sui, Q. Wu, X. Liu, D. Huang, High performance piezoelectric nanogenerator with silver nanowires embedded in polymer matrix for mechanical energy harvesting. Ceram. Int. **47**, 35096–35104 (2021). https://doi.org/10.1016/j.ceramint.2021.09.052

41. P. Martins, A. Lopes, S. Lanceros-Mendez, Electroactive phases of poly (vinylidene fluoride): determination, processing and applications. Prog. Polym. Sci. **39**, 683–706 (2014). https://doi.org/10.1016/j.progpolymsci.2013.07.006

42. R. Bhunia, S. Gupta, B. Fatma, Prateek, R.K. Gupta, A. Garg, Milli-watt power harvesting from dual triboelectric and piezoelectric effects of multifunctional green and robust reduced graphene oxide/P (VDF-TrFE) composite flexible films. ACS Appl. Mater. Interfaces **11**, 38177–38189 (2019). https://doi.org/10.1021/acsami.9b13360

43. S. Ojha, S. Paria, S.K. Karan, S.K. Si, A. Maitra, A.K. Das, L. Halder, A. Bera, A. De, B.B. Khatua, Morphological interference of two different cobalt oxides derived from a hydrothermal protocol and a single two-dimensional metal organic framework precursor to stabilize the β-phase of PVDF for flexible piezoelectric nanogenerators. Nanoscale

11, 22989–22999 (2019). https://doi.org/10.1039/C9NR08315D

44. F. Mokhtari, G.M. Spinks, S. Sayyar, J. Foroughi, Dynamic mechanical and creep behaviour of meltspun pvdf nanocomposite fibers. Nanomaterials **11**, 2153 (2021). https://doi.org/10.3390/nano11082153

45. M.T. Ong, E.J. Reed, Engineered piezoelectricity in graphene. ACS nano **6**, 1387–1394 (2012). https://doi.org/10.1021/nn204198g

46. K. Shi, B. Sun, X. Huang, P. Jiang, Synergistic effect of graphene nanosheet and BaTiO$_3$ nanoparticles on performance enhancement of electrospun PVDF nanofiber mat for flexible piezoelectric nanogenerators. Nano Energy **52**, 153–162 (2018). https://doi.org/10.1016/j.nanoen.2018.07.053

47. S. Niu, X. Wang, F. Yi, Y.S. Zhou, Z.L. Wang, A universal self-charging system driven by random biomechanical energy for sustainable operation of mobile electronics. Nat. Commun. **6**, 8975 (2015). https://doi.org/10.1038/ncomms9975

48. Y. Zou, V. Raveendran, J. Chen, Wearable triboelectric nanogenerators for biomechanical energy harvesting. Nano Energy **77**, 105303 (2020). https://doi.org/10.1016/j.nanoen.2020.105303

49. T. He, H. Wang, J. Wang, X. Tian, F. Wen, Q. Shi, J.S. Ho, C. Lee, Self-sustainable wearable textile nano-energy nano-system (NENS) for next-generation healthcare applications. Adv. Sci. **6**, 1901437 (2019). https://doi.org/10.1002/advs.201901437